

# Constraining primordial non-Gaussianity by combining photometric galaxy and 21cm intensity mapping surveys

Mponeng Kopana<sup>1</sup>, Sheean Jolicoeur<sup>2</sup>, Roy Maartens<sup>1,3,4</sup>

<sup>1</sup>Department of Physics & Astronomy, University of the Western Cape, Cape Town 7535, South Africa

<sup>2</sup>Department of Physics, Stellenbosch University, Matieland 7602, South Africa

<sup>3</sup>Institute of Cosmology & Gravitation, University of Portsmouth, Portsmouth PO1 3FX, United Kingdom

<sup>4</sup>National Institute for Theoretical & Computational Sciences (NITheCS), Cape Town 7535, South Africa

**Abstract.** The fluctuations produced during cosmic inflation may exhibit non-Gaussian characteristics that are imprinted in the large-scale structure of the Universe. This non-Gaussian imprint is an ultra-large scale signal that can be detected using the power spectrum. We focus on the local-type non-Gaussianity  $f_{\text{NL}}$  and employ a multi-tracer analysis that combines different probes in order to mitigate cosmic variance and maximize the non-Gaussian signal. In our previous paper, we showed that combining spectroscopic galaxy surveys with 21 cm intensity mapping surveys in interferometer mode could lead to a  $\sim 20\text{-}30\%$  improvement in the precision on this non-Gaussian signal. Here we combine the same 21 cm experiments, including also single-dish surveys, with photometric galaxy surveys. The 21 cm single-dish surveys are based on MeerKAT and SKAO and the interferometric surveys are alike to HIRAX and PUMA. We implement foreground-avoidance filters and utilize models for the 21 cm thermal noise associated with single-dish and interferometer modes. The photometric galaxy surveys are similar to the DES and LSST. Our multi-tracer Fisher forecasts show a better precision for the combination of the photometric galaxy surveys and 21 cm interferometric surveys than with the 21 cm single-dish surveys - leading to at most an improvement of 23% in the former case and 16% in the latter case. Furthermore, we examine the impact of varying the foreground filter parameter, redshift range and sky area on the derived constraint. We find that the  $f_{\text{NL}}$  constraint is highly sensitive to both the redshift range and sky area. The foreground filter parameter shows negligible effect.

---

## Contents

|          |   |           |
|----------|---|-----------|
| <b>1</b> | <b>Introduction</b>                         | <b>1</b>  |
| <b>2</b> | <b>Galaxy and intensity power spectra</b>   | <b>2</b>  |
| <b>3</b> | <b>Galaxy and intensity mapping surveys</b> | <b>3</b>  |
| <b>4</b> | <b>Noise power spectra</b>                  | <b>5</b>  |
| <b>5</b> | <b>Fisher forecast</b>                      | <b>7</b>  |
| <b>6</b> | <b>Results</b>                              | <b>8</b>  |
| <b>7</b> | <b>Conclusions</b>                          | <b>14</b> |

---

## 1 Introduction

In the standard model of cosmology, Inflation leads to the generation of primordial density fluctuations, which serve as the seeds for the large-scale structure observed today. For the simplest slow-roll single-field Inflation models, the primordial fluctuations are nearly Gaussian, but in many other Inflation models, fluctuations exhibit non-Gaussianity, which leaves distinct imprints on the cosmic microwave background (CMB) and the large-scale structure. These imprints provide a powerful probe of the primordial Universe [1–4]. Local PNG peaks in the squeezed configurations and thereby leaves an imprint, via scale-dependent bias, in the power spectrum of biased tracers of the dark matter [5, 6]. The strongest current constraints on the local PNG parameter  $f_{\text{NL}}$  are from the CMB bispectrum measured by the Planck survey:  $f_{\text{NL}} = -0.9 \pm 5.1$  at the 68% confidence level [7]. This precision is much greater than recent galaxy survey measurements (e.g. [8]). Future CMB surveys (e.g. [9, 10]), will improve this precision, but not enough to achieve  $\sigma(f_{\text{NL}}) < 1$ , which would allow us to rule out a large body of Inflation models [11].

Upcoming galaxy surveys (e.g. [12, 13]) and neutral hydrogen (HI) intensity mapping surveys (e.g. [14–16]) will encompass many more modes than CMB surveys, opening up the prospect of higher precision measurements of  $f_{\text{NL}}$ . However, using only the power spectrum of a single tracer is unlikely to achieve  $\sigma(f_{\text{NL}}) < 1$  because of the growth of cosmic variance on ultra-large scales [17, 18]. A work-around to this obstacle is the multi-tracer method, which suppresses cosmic variance [14, 19–38].

In our previous work [38] we used multi-tracer Fourier power spectra to combine the HI intensity maps from interferometric surveys similar to those expected from HIRAX [15] and PUMA [16], with spectroscopic galaxy surveys similar to those expected from Euclid [13] and MegaMapper [39]. This paper is a follow-up where we use the same HI intensity mapping surveys but also include single-dish surveys similar to those expected from MeerKAT [40] and SKA [14] – and we combine these HI intensity maps with photometric galaxy samples similar to those expected from DES [41] and LSST [42]. Although photometric surveys lose accuracy in redshift space, this is less important for PNG constraints than the higher number densities in the photometric case [14, 17, 23, 24].

## 2 Galaxy and intensity power spectra

For a dark matter tracer  $A$ , the clustering bias in the presence of local PNG is

$$b_A^{\text{nG}}(z, k) = b_A(z) + b_{A\phi}(z) \frac{f_{\text{NL}}}{\mathcal{M}(z, k)}, \quad \mathcal{M}(z, k) = \frac{2}{3\Omega_{m0}H_0^2} \frac{D(z)}{g_{\text{in}}} T(k) k^2, \quad (2.1)$$

where  $b_A$  is the Gaussian clustering bias. The primordial non-Gaussian bias, following [43], is assumed to be

$$b_{A\phi}(z) = 2\delta_c [b_A(z) - p_A], \quad p_A = 0.955, \quad (2.2)$$

where the critical matter overdensity is  $\delta_c = 1.686$ . (For further discussion of  $b_{A\phi}$ , see e.g. [35, 44–47].) In (2.1),  $T(k)$  is the matter transfer function (normalized to 1 on very large scales),  $D$  is the growth factor (normalized to 1 today) and  $g_{\text{in}} = (1 + z_{\text{in}})D_{\text{in}}$  is the initial growth suppression factor, with  $z_{\text{in}}$  deep in the matter era. In  $\Lambda$ CDM with Planck best-fit parameters [48],  $g_{\text{in}} = 1.274$ .

Then the galaxy number density contrast,  $\delta_g = \delta n_g / \bar{n}_g$ , or the HI brightness temperature contrast,  $\delta_{\text{HI}} = \delta T_{\text{HI}} / \bar{T}_{\text{HI}}$ , can be expressed in the general form

$$\delta_A(z, \mathbf{k}) = E_A(z, \mathbf{k}) \left[ b_A^{\text{nG}}(z, k) + f(z)\mu^2 \right] \delta(z, \mathbf{k}), \quad (2.3)$$

where  $f(z) = -d \ln D(z) / d \ln(1 + z)$  is the growth rate,  $\mu = \hat{\mathbf{k}} \cdot \mathbf{n}$ ,  $\delta$  is the matter density contrast and  $E_A$  is a tracer-dependent factor. For galaxies,  $E_g$  accounts for photometric redshift errors,

$$E_g = \exp \left\{ - \frac{k^2 \mu^2 [\sigma_{z0}(1 + z)]^2}{2H^2} \right\}, \quad (2.4)$$

where  $\sigma_{z0}$  is the root-mean-square (RMS) redshift error of the galaxy survey at  $z = 0$  [49–51].

For HI intensity,  $E_{\text{HI}}$  accounts for foreground avoidance and telescope beam effects:

$$E_{\text{HI}} = \mathcal{FB}, \quad (2.5)$$

where the foreground and beam factors depend on whether the HI intensity map is made in interferometer or single-dish mode. In the case of the foreground factor:

$$\mathcal{F} = \mathcal{F}_{\text{radial}} \mathcal{F}_{\text{wedge}} = \left[ 1 - \exp \left\{ - \mu^2 \left( \frac{k}{k_{\text{fg}}} \right)^2 \right\} \right] \mathcal{F}_{\text{wedge}}. \quad (2.6)$$

The radial damping term affects both single-dish and interferometer surveys. It models the loss of large-scale radial wave-modes due to foreground contamination [52–55]. We use  $k_{\text{fg}} = 0.005$  and  $0.01 h/\text{Mpc}$ . The term  $\mathcal{F}_{\text{wedge}}$  is 1 for single-dish surveys. For interferometer surveys, there is additional foreground contamination in a wedge-shaped region of  $\mathbf{k}$ -space defined by [16, 56–61]:

$$|k_{\parallel}| < W(z) k_{\perp}, \quad (2.7)$$

$$W(z) = r(z) \mathcal{H}(z) \sin [0.61 N_w \theta_{\text{fov}}(z)]. \quad (2.8)$$

Here  $k_{\parallel} = \mu k$ ,  $k_{\perp} = (1 - \mu^2)^{1/2} k$ ,  $r$  is the comoving radial distance,  $\mathcal{H} = H/(1 + z)$  is the conformal Hubble rate and  $\theta_{\text{fov}} = 1.22 \lambda_{21}(1 + z)/D_d$  is the field of view, with  $D_d$  the dish

diameter. The extent of foreground contamination is determined by the number of primary beams affected,  $N_w$ . We choose  $N_w = 1$ . For interferometer surveys,  $\mathcal{F}_{\text{wedge}}$  in (2.6) is the Heaviside step function,

$$\mathcal{F}_{\text{wedge}} = \Theta(|k_{\parallel}| - W(z) k_{\perp}). \quad (2.9)$$

Figure 1 illustrates  $\mathcal{F}_{\text{radial}}$  and the wedge region (2.8). The beam factor  $\beta$  in (2.5) depends on whether the HI intensity map is made in interferometer or single-dish mode:

$$\text{interferometer mode: } \beta = \theta_{\text{fov}} \quad (2.10)$$

$$\text{single-dish mode: } \beta = \exp\left(-\frac{k_{\perp}^2 r^2 \theta_{\text{fov}}^2}{16 \ln 2}\right), \quad (2.11)$$

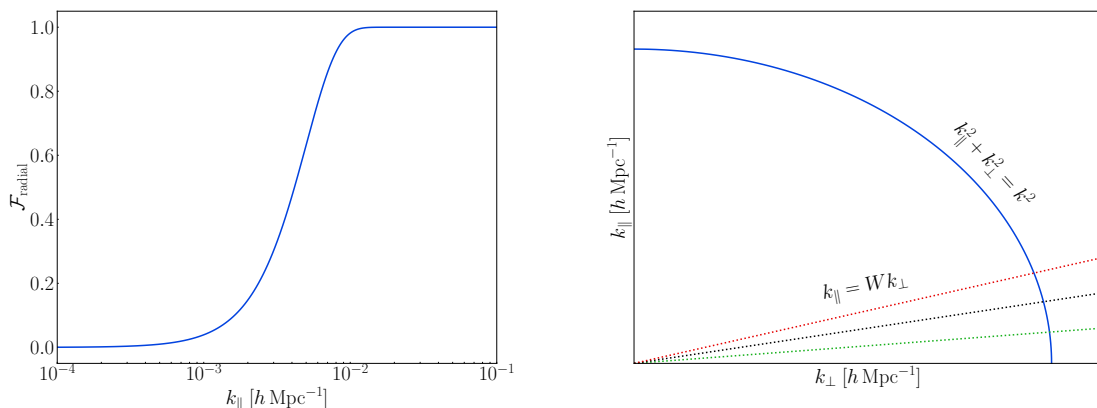


**Figure 1.** For HI intensity mapping: radial foreground damping function (*left*); interferometer foreground wedge region, whose size increases with redshift (*right*).

The power spectra are given by

$$\langle \delta_A(z, \mathbf{k}) \delta_B(z, \mathbf{k}') \rangle = (2\pi)^3 P_{AB}(z, \mathbf{k}) \delta^D(\mathbf{k} + \mathbf{k}'), \quad (2.12)$$

so that

$$P_{AB} = E_A E_B (b_A^{\text{nG}} + f\mu^2) (b_B^{\text{nG}} + f\mu^2) P, \quad (2.13)$$

where  $P$  is the matter power spectrum (computed with CLASS [62]). When  $B = A$  we use the shorthand  $P_A \equiv P_{AA}$ .

### 3 Galaxy and intensity mapping surveys

In this paper, our aim is not to produce forecasts for specific surveys, but rather to estimate the improvements in precision that are possible with a multi-tracer analysis. To this end, we consider mock surveys which combine very different pairs of tracers: a photometric galaxy sample and an HI intensity map. The basic properties assumed for the mock surveys are similar to those of surveys considered in the literature:

- Photometric galaxy samples D and L, similar to those from DES (blue and red) [41] and LSST (blue) [42] respectively.

**Table 1.** Specifications of mock surveys. Here D, L, M, S, H, P have properties similar to DES, LSST, MeerKAT (UHF Band), SKA (Band 1), HIRAX, PUMA respectively.

| HI single-dish $\otimes$ Photometric    | $z$        | $\Omega_{\text{sky}}$ [deg <sup>2</sup> ] | $t_{\text{tot}}$ [hr] |
|---|------------|---|-----------------------|
| M $\otimes$ D                           | 0.4 – 1.45 | 5,000                                     | 4,000                 |
| S $\otimes$ D                           | 0.35 – 2.0 | 5,000                                     | 2,500                 |
| S $\otimes$ L                           | 0.35 – 2.9 | 10,000                                    | 5,000                 |
| HI interferometer $\otimes$ Photometric |            |   |                       |
| H $\otimes$ D                           | 0.8 – 2.0  | 5,000                                     | 5,833                 |
| H $\otimes$ L                           | 0.8 – 2.5  | 10,000                                    | 12,000                |
| P $\otimes$ L                           | 0.3 – 2.9  | 10,000                                    | 19,000                |

- HI intensity mapping samples:
  - single-dish mode samples M and S, similar to those from MeerKAT (UHF Band) [40] and SKA-MID (Band 1) [14] respectively;
  - interferometer mode samples H and P, similar to those from HIRAX [15] and PUMA [16] respectively.

Table 1 summarises the basic survey specifications that we assume. Note that for each multi-tracer pair and for the single tracers in the pair, we only consider the overlapping sky area and redshift range – since our focus is on the improvement delivered by the multi-tracer analysis. In the case of future surveys we assume a nominal overlap sky area of 10,000 deg<sup>2</sup>.

The Gaussian clustering bias for galaxies and intensity maps is assumed known up to an overall amplitude parameter, following [63]:

$$b_A(z) = b_{A0} \beta_A(z). \quad (3.1)$$

For the photometric D and L samples we assume

$$b_D(z) = b_{D0}(1 + 0.84z) \quad \text{fiducial } b_{D0} = 1.0 \quad [25], \quad (3.2)$$

$$b_L(z) = b_{L0}/D(z) \quad \text{fiducial } b_{L0} = 0.95 \quad [23]. \quad (3.3)$$

For the photometric surveys we assume

$$\sigma_{z0} = 0.05. \quad (3.4)$$

All HI intensity surveys have the same Gaussian clustering bias. Following [64] we assume

$$b_{\text{HI}}(z) = b_{\text{HI}0}(1 + 0.823z - 0.0546z^2) \quad \text{fiducial } b_{\text{HI}0} = 0.842. \quad (3.5)$$

For the L sample, we use the background comoving number density for LSST given in Table 8 of [51]. For the D sample, we use the fitting formula for the DES number per redshift

per solid angle [25, 65]:

$$\bar{N}_D(z) = 8.05 \times 10^4 \left( \frac{z}{0.57} \right)^{1.04} \exp \left[ - \left( \frac{z}{0.57} \right)^{1.34} \right] \text{ deg}^{-2}. \quad (3.6)$$

Then the comoving number density is given by

$$\bar{n}_D = \frac{(1+z)\mathcal{H}}{r^2} \bar{N}_D. \quad (3.7)$$

The background brightness temperature is the same for all HI intensity samples and we model it as [40]:

$$\bar{T}_{\text{HI}}(z) = 0.0559 + 0.2324 z - 0.0241 z^2 \text{ mK}. \quad (3.8)$$

The Gaussian clustering biases and number densities for L (LSST-like) and D (DES-like) are displayed in Figure 2. Figure 3 displays the HI intensity Gaussian bias and the background brightness temperature.

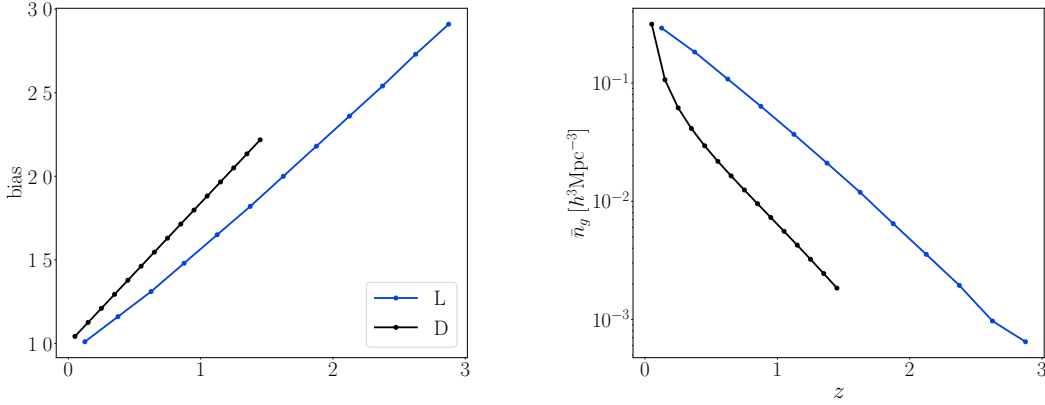


**Figure 2.** Galaxy surveys: Gaussian clustering biases (*left*); comoving number densities (*right*).

## 4 Noise power spectra

The measured tracer power spectrum is made up of the cosmological signal and the noise, so that the total observed auto-power is

$$\tilde{P}_A = P_A + P_{A \text{ noise}}. \quad (4.1)$$

For galaxy surveys,  $A = g$ , the noise power spectrum is dominated by shot noise:

$$P_{g \text{ noise}} = \frac{1}{\bar{n}_g}. \quad (4.2)$$

For HI intensity mapping surveys,  $A = \text{HI}$ , on the linear scales that we consider, the noise power is dominated by the thermal noise and shot noise can be neglected [64, 66]. The shot

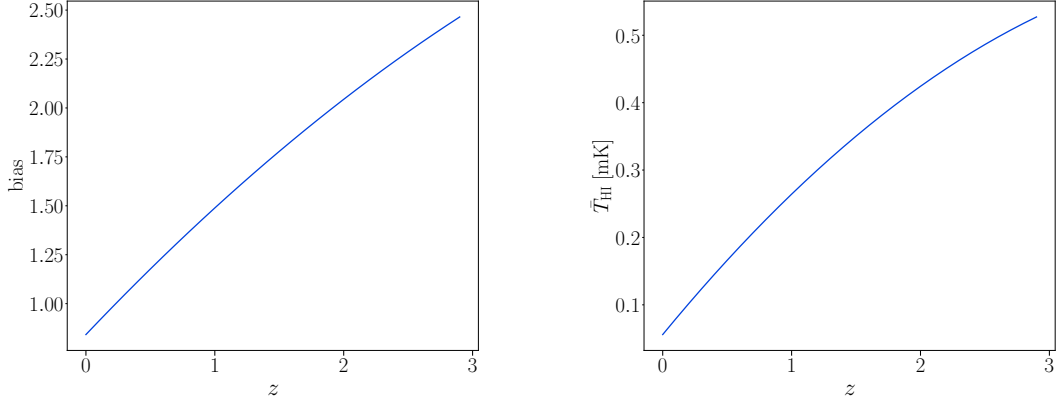


**Figure 3.** HI intensity maps: Gaussian clustering bias (*left*); background brightness temperature (*right*).

noise cross-power between HI intensity and galaxy surveys can also be neglected [33, 67]. Since HI thermal noise does not correlate with galaxy shot noise, we neglect the noise cross-power:

$$\tilde{P}_{g\text{HI}} = P_{g\text{HI}}. \quad (4.3)$$

For HI intensity mapping surveys, the thermal noise power spectrum is [16, 59, 68, 69]:

$$P_{\text{HI noise}} = \frac{\lambda_{21} \Omega_{\text{sky}}}{2t_{\text{tot}}} \frac{(1+z)r^2}{\mathcal{H}} \left( \frac{T_{\text{sys}}}{\bar{T}_{\text{HI}}} \right)^2 \alpha, \quad (4.4)$$

where we used natural units (speed of light = 1) and

$$\text{single-dish mode: } \alpha = \frac{1}{N_{\text{d}}}, \quad (4.5)$$

$$\text{interferometer mode: } \alpha = \left[ \frac{4\lambda_{21}(1+z)}{0.7\pi D_{\text{d}}^2} \right]^2 \frac{1}{n_{\text{b}}^{\text{phys}}}. \quad (4.6)$$

Here  $N_{\text{d}}$  is the number of dishes and the system temperature is [16]:

$$T_{\text{sys}} = T_{\text{d}} + T_{\text{sky}} = T_{\text{d}} + 2.7 + 25 \left[ \frac{400 \text{ MHz}}{\nu_{21}} (1+z) \right]^{2.75} \text{ K}, \quad (4.7)$$

where  $T_{\text{d}}$  is the dish receiver temperature. All specifications are given in Table 2.

The physical baseline density of the HIRAX- and PUMA-like surveys is modelled following [16]:

$$n_{\text{b}}^{\text{phys}} = \left( \frac{N_{\text{s}}}{D_{\text{d}}} \right)^2 \frac{a + b(L/L_{\text{s}})}{1 + c(L/L_{\text{s}})^d} \exp[-(L/L_{\text{s}})^e], \quad L = \frac{k_{\perp} r}{2\pi} \lambda_{21}(1+z). \quad (4.8)$$

H (HIRAX-like) is a square close-packed array, whereas P (PUMA-like) is a hexagonal close-packed array with a 50% fill factor – meaning that dish sites occupy half of the total area [16, 61]. Then it follows that  $N_{\text{s}}^2 = N_{\text{d}}$  for H and  $N_{\text{s}}^2 = 2N_{\text{d}}$  for P [16, 70], where  $L_{\text{s}} = N_{\text{s}} D_{\text{d}}$ . The values of the fitting parameters  $a, b, c, d, e$  in (4.8) are given in Table 2, from [16] (their Appendix D, last equation). See Figure 4 for plots of the baseline density.

**Table 2.** Specifications of HI intensity mapping surveys: M (MeerKAT-like), S (SKA-like), H (HIRAX-like), P (PUMA-like).  $N_d$  is the number of dishes,  $D_d$  is the dish diameter,  $T_d$  is the dish receiver temperature,  $D_{\max}$  is the maximum baseline (for interferometer surveys),  $t_{\text{tot}}$  is the observing time. The interferometer parameters  $N_s$  and  $a, \dots, e$  appear in (4.8).

| Survey             | $N_d$     | $N_s$    | $T_d$<br>[K] | $D_d$<br>[m] | $D_{\max}$<br>[m] |
|--------------------|-----------|----------|--------------|--------------|-------------------|
| M                  | 64        | -        | 25           | 13.5         | -                 |
| S                  | 197       | -        | 25           | 15           | -                 |
| H(256, 1024)       | 256, 1024 | 16, 32   | 50           | 6            | 141, 282          |
| P(5k, 32k)         | 5k, 32k   | 100, 253 | 93           | 6            | 648, 1640         |
| Fitting parameters | $a$       | $b$      | $c$          | $d$          | $e$               |
| H(256, 1024)       | 0.4847    | -0.3300  | 1.3157       | 1.5974       | 6.8390            |
| P(5k, 32k)         | 0.5698    | -0.5274  | 0.8358       | 1.6635       | 7.3177            |

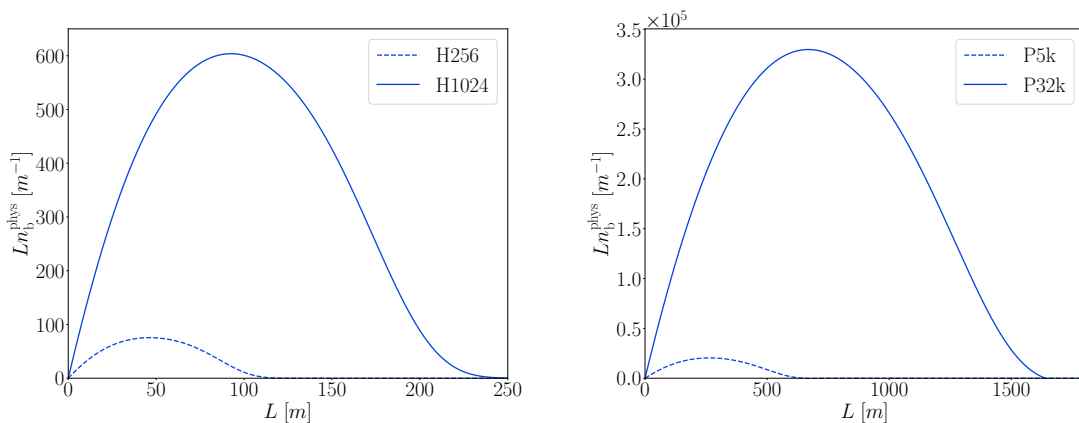


**Figure 4.** Physical baseline density for HI IM surveys: HIRAX-like (*left*) and PUMA-like (*right*).

## 5 Fisher forecast

Three cosmological and two nuisance parameters,

$$\vartheta_\alpha = \{f_{\text{NL}}, A_s, n_s, b_{g0}, b_{\text{HI0}}\}, \quad (5.1)$$

are considered, with fiducial values for the LCDM cosmological parameters given by the *Planck 2018* best-fit values [48], including  $\bar{A}_s = 2.105 \times 10^{-9}$  and  $\bar{n}_s = 0.9665$ . We assume that the PNG fiducial is  $\bar{f}_{\text{NL}} = 0$  and the fiducial values of  $b_{A_0}$  are given in (3.2), (3.3) and (3.5).

The Fisher information matrix in each redshift bin is

$$F_{\alpha\beta}^{\mathbf{P}} = \sum_{\mu=-1}^{+1} \sum_{k=k_{\min}}^{k_{\max}} \partial_\alpha \mathbf{P} \cdot \text{Cov}(\mathbf{P}, \mathbf{P})^{-1} \cdot \partial_\beta \mathbf{P}^T. \quad (5.2)$$



Here  $\partial_\alpha = \partial/\partial\theta_\alpha$ , the data vector of power spectra is

$$\mathbf{P} = (P_g, P_{g\text{HI}}, P_{\text{HI}}), \quad (5.3)$$

and the covariance is [71–74]:

$$\text{Cov}(\mathbf{P}, \mathbf{P}) = \frac{k_f^3}{2\pi k^2 \Delta k} \frac{2}{\Delta\mu} \begin{pmatrix} \tilde{P}_g^2 & \tilde{P}_g \tilde{P}_{g\text{HI}} & \tilde{P}_{g\text{HI}}^2 \\ \tilde{P}_g \tilde{P}_{g\text{HI}} & \frac{1}{2}(\tilde{P}_g \tilde{P}_{\text{HI}} + \tilde{P}_{g\text{HI}}^2) & \tilde{P}_{\text{HI}} \tilde{P}_{g\text{HI}} \\ \tilde{P}_{g\text{HI}}^2 & \tilde{P}_{\text{HI}} \tilde{P}_{g\text{HI}} & \tilde{P}_{\text{HI}}^2 \end{pmatrix}. \quad (5.4)$$

We choose

$$\Delta z = 0.1, \quad \Delta\mu = 0.04, \quad \Delta k = k_f = 2\pi V^{-1/3}, \quad k_{\text{max}} = 0.08(1+z)^{2/(2+n_s)} h/\text{Mpc}, \quad (5.5)$$

where  $V$  is the volume of the bin and

$$A = g : k_{\text{min}} = k_f, \quad A = \text{HI} : k_{\text{min}} = \max(k_f, k_{\text{fg}}). \quad (5.6)$$

## 6 Results

**Table 3.** Marginalised 68% CL errors on  $f_{\text{NL}}$  from galaxy surveys D (DES-like), L (LSST-like) and HI IM single dish-mode surveys A = M (MeerKAT UHF-like), S (SKA Band 1-like).

| M $\otimes$ D           |                         | S $\otimes$ D           |                         | S $\otimes$ L           |                         |
|-------------------------|-------------------------|-------------------------|-------------------------|-------------------------|-------------------------|
| Survey A, A $\otimes$ B | $\sigma(f_{\text{NL}})$ | Survey A, A $\otimes$ B | $\sigma(f_{\text{NL}})$ | Survey A, A $\otimes$ B | $\sigma(f_{\text{NL}})$ |
| D                       | 13.0                    | D                       | 6.89                    | L                       | 2.28                    |
| M                       | 22.5                    | S                       | 10.9                    | S                       | 4.15                    |
| M $\otimes$ D           | 10.3                    | S $\otimes$ D           | 5.78                    | S $\otimes$ L           | 2.15                    |

The main results are presented in Table 3 and Table 4, showing the errors on  $f_{\text{NL}}$  for HI intensity mapping surveys combined with photometric surveys, after marginalising over  $A_s, n_s$  and the nuisance parameters  $b_{A0}$ . We consider multi-tracer combinations of the form HI intensity  $\otimes$  galaxy, using HI surveys M (like MeerKAT UHF Band) and S (like SKA Band 1) in single-dish mode, and H (HIRAX-like) and P (PUMA-like) in interferometer mode, combined with galaxy surveys D (DES-like) and L (LSST-like).

We adjusted the HI intensity observational time in each case to be consistent with the overlapping sky area and redshift range. For each multi-tracer scenario A  $\otimes$  B, we used the same sky area and redshift range for the two single-tracers and the multi-tracer. We omitted the case P  $\otimes$  D, because of poor overlap in redshift. Note that the full sky area and redshift range of each survey are not used in every multi-tracer combination – since we only use the *overlapping* sky area and redshift range. This explains for example why D (DES-like) achieves better precision than S (SKA-like) – since D in the multi-tracer is the full DES-like survey, while S is only a fraction of the full SKA-like survey.

**Table 4.** Marginalised 68% CL errors on  $f_{\text{NL}}$  from galaxy surveys A = D (DES-like), L (LSST-like) and HI IM inteferometer-mode surveys A = H (HIRAX-like) and P (PUMA-like). H and P have phases 1 and 2 with the initial and final number of dishes.

| H $\otimes$ D           |                         | H $\otimes$ L           |                         | P $\otimes$ L           |                         |
|-------------------------|-------------------------|-------------------------|-------------------------|-------------------------|-------------------------|
| Survey A, A $\otimes$ B | $\sigma(f_{\text{NL}})$ | Survey A, A $\otimes$ B | $\sigma(f_{\text{NL}})$ | Survey A, A $\otimes$ B | $\sigma(f_{\text{NL}})$ |
| D                       | 7.00                    | L                       | 2.92                    | L                       | 2.22                    |
| H256                    | 11.40                   | H256                    | 5.15                    | P5k                     | 2.48                    |
| H1024                   | 9.09                    | H1024                   | 4.03                    | P32k                    | 2.28                    |
| H256 $\otimes$ D        | 5.70                    | H256 $\otimes$ L        | 2.61                    | P5k $\otimes$ L         | 1.85                    |
| H1024 $\otimes$ D       | 5.40                    | H1024 $\otimes$ L       | 2.51                    | P32k $\otimes$ L        | 1.81                    |

The results clearly demonstrate the improvement in precision on local PNG from the multi-tracer. At higher redshifts, such as those covered by SKA-like (Table 3) and HIRAX- and PUMA-like (Table 4), the improvement in precision is more notable, especially for SKA- and PUMA-like, due to the large sky volumes probed.

We also note that the first phases of HIRAX (256 dishes) and PUMA (5k dishes) perform nearly as well in the multi-tracer as the second phases. A high number of dishes for these interferometers is not necessary for  $f_{\text{NL}}$  constraints.

The  $\sigma(f_{\text{NL}})$  results in Table 3 and Table 4 are cumulative – and they use the optimistic value of the radial foreground avoidance parameter,  $k_{\text{fg}} = 0.005 h/\text{Mpc}$ . The per-bin constraints are shown in Figure 5 and Figure 6, for the optimistic and less optimistic values  $k_{\text{fg}} = 0.005, 0.01 h/\text{Mpc}$ .

In Table 5, we present the results of the multi-tracer analysis for the particular example of H256  $\otimes$  L, illustrating how effectively the multi-tracer approach can mitigate the effects of foreground removal when estimated at a fiducial value of  $k_{\text{fg}} = 0.005 h/\text{Mpc}$  or a less optimistic value of  $k_{\text{fg}} = 0.01 h/\text{Mpc}$ . We vary the overlapping sky area and fix the overlapping redshift range to the fiducial  $0.8 \leq z \leq 2.5$  (top of the Table). Then we vary the overlapping redshift range at fixed overlapping sky area 10,000 deg<sup>2</sup> (bottom of the Table). The results indicate that as the sky area coverage or redshift range decreases, the impact of the foreground effect becomes more noticeable.

Figure 7 and Figure 8 present the  $1\sigma$  (68%) error contours for  $f_{\text{NL}}$ ,  $n_s$  and  $A_s$ , marginalising over  $b_{A0}$ . It is evident that HI intensity mapping offers stronger constraints on  $n_s$  and  $A_s$  than photometric surveys, although it provides weaker constraints on  $f_{\text{NL}}$ .

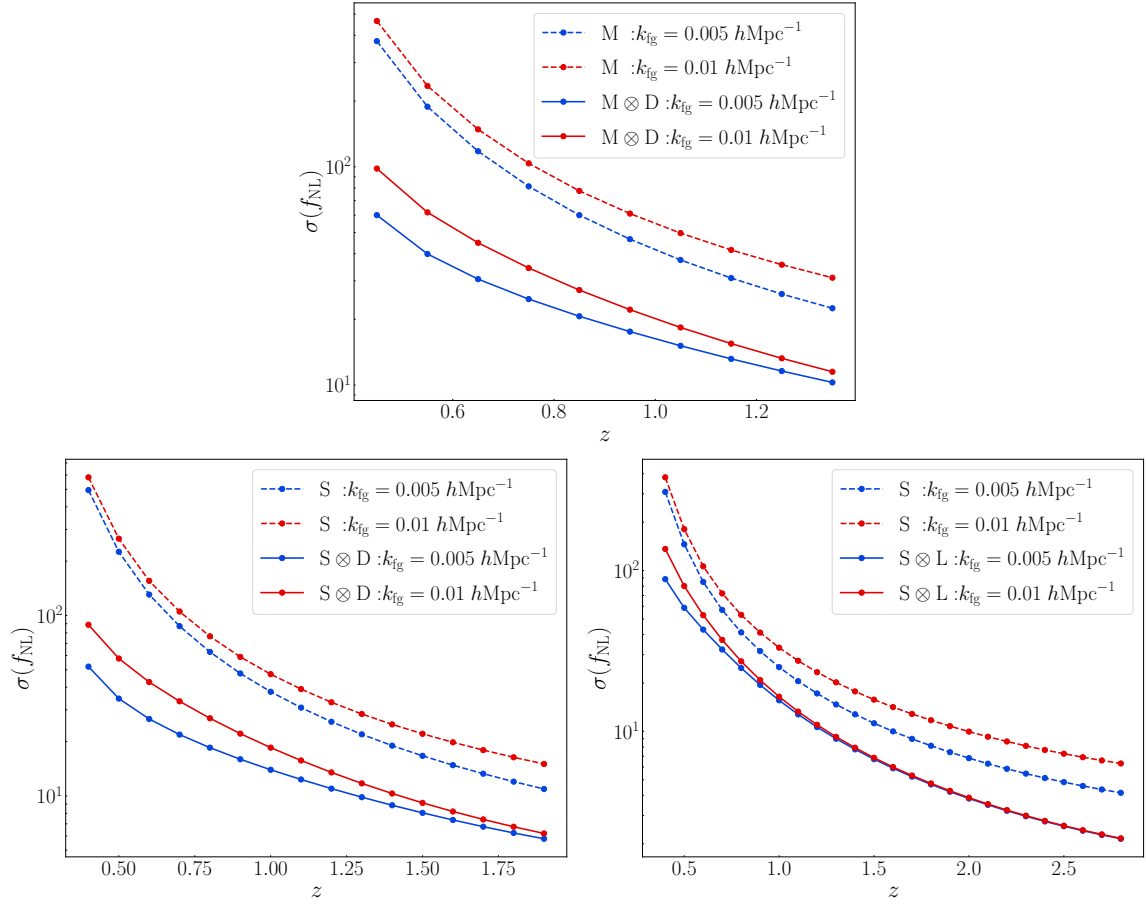


**Figure 5.** Cumulative errors on  $f_{\text{NL}}$  for the multi-tracer involving single-dish mode HI intensity maps. Results are shown for the two cases of foreground loss,  $k_{\text{fg}} = 0.005, 0.01 \text{ h/Mpc}$ .

**Table 5.** Marginalized 68% (CL) errors on  $f_{\text{NL}}$  are analyzed against the estimated surveyed area and redshift ranges for the multi-tracer combination of H256 (HIRAX-like) and L (LSST-like) when  $k_{\text{fg}} = 0.005 \text{ hMpc}^{-1}$  and  $k_{\text{fg}} = 0.01 \text{ hMpc}^{-1}$ .

| H256 $\otimes$ L  |           |           |           |
|---|-----------|-----------|-----------|
| $\Omega_{\text{sky}} [\text{deg}^2]$                              | 5,000     | 10,000    | 15,000    |
| $\sigma(f_{\text{NL}}) [k_{\text{fg}} = 0.005 \text{ hMpc}^{-1}]$ | 4.13      | 2.61      | 1.99      |
| $\sigma(f_{\text{NL}}) [k_{\text{fg}} = 0.01 \text{ hMpc}^{-1}]$  | 4.15      | 2.62      | 2.00      |
| $z$   | 0.8 – 1.5 | 0.8 – 2.0 | 0.8 – 2.5 |
| $\sigma(f_{\text{NL}}) [k_{\text{fg}} = 0.005 \text{ hMpc}^{-1}]$ | 7.53      | 3.99      | 2.61      |
| $\sigma(f_{\text{NL}}) [k_{\text{fg}} = 0.01 \text{ hMpc}^{-1}]$  | 7.58      | 4.01      | 2.62      |

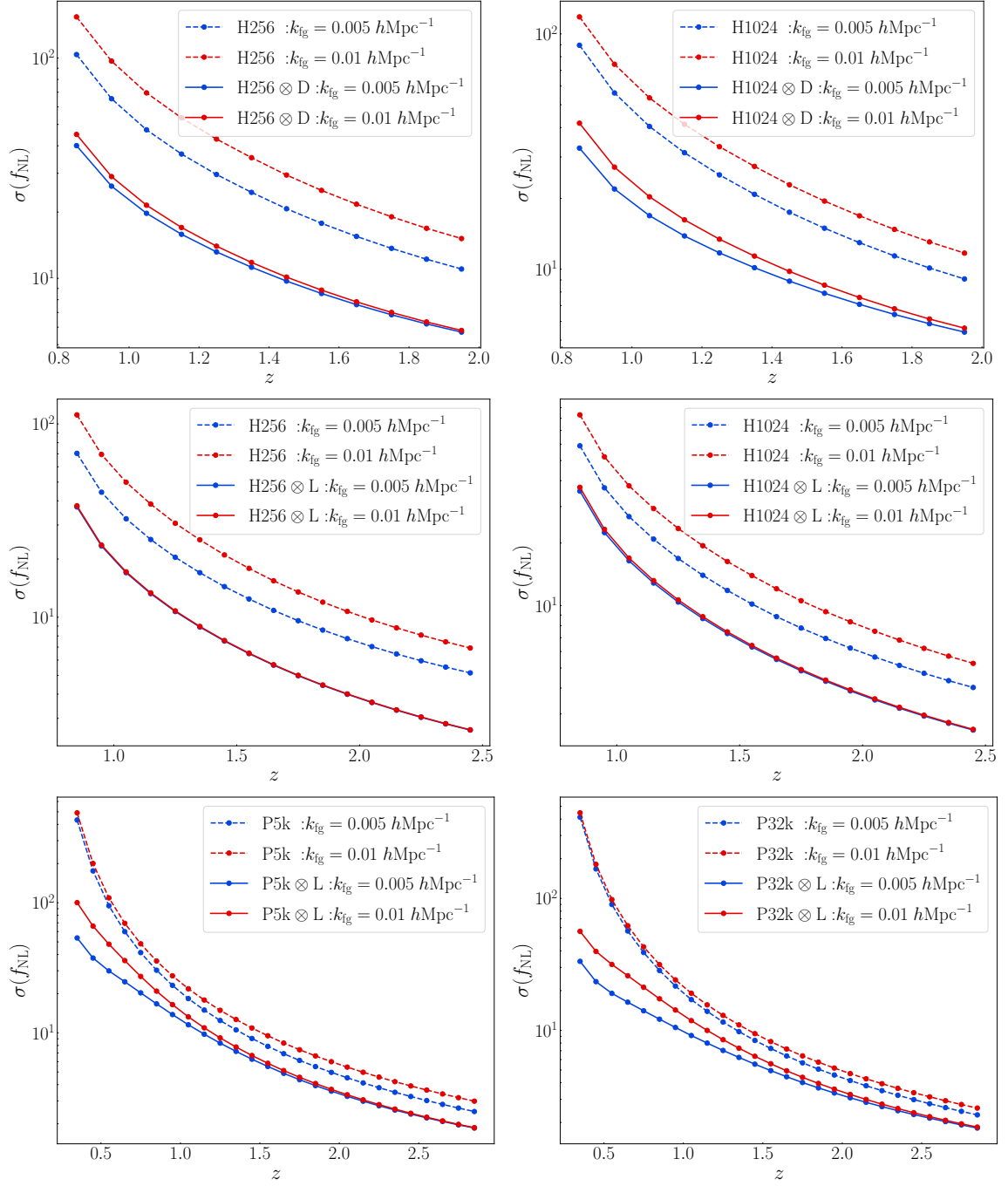


**Figure 6.** As in [Figure 5](#) for the case of HI intensity maps in interferometer mode.

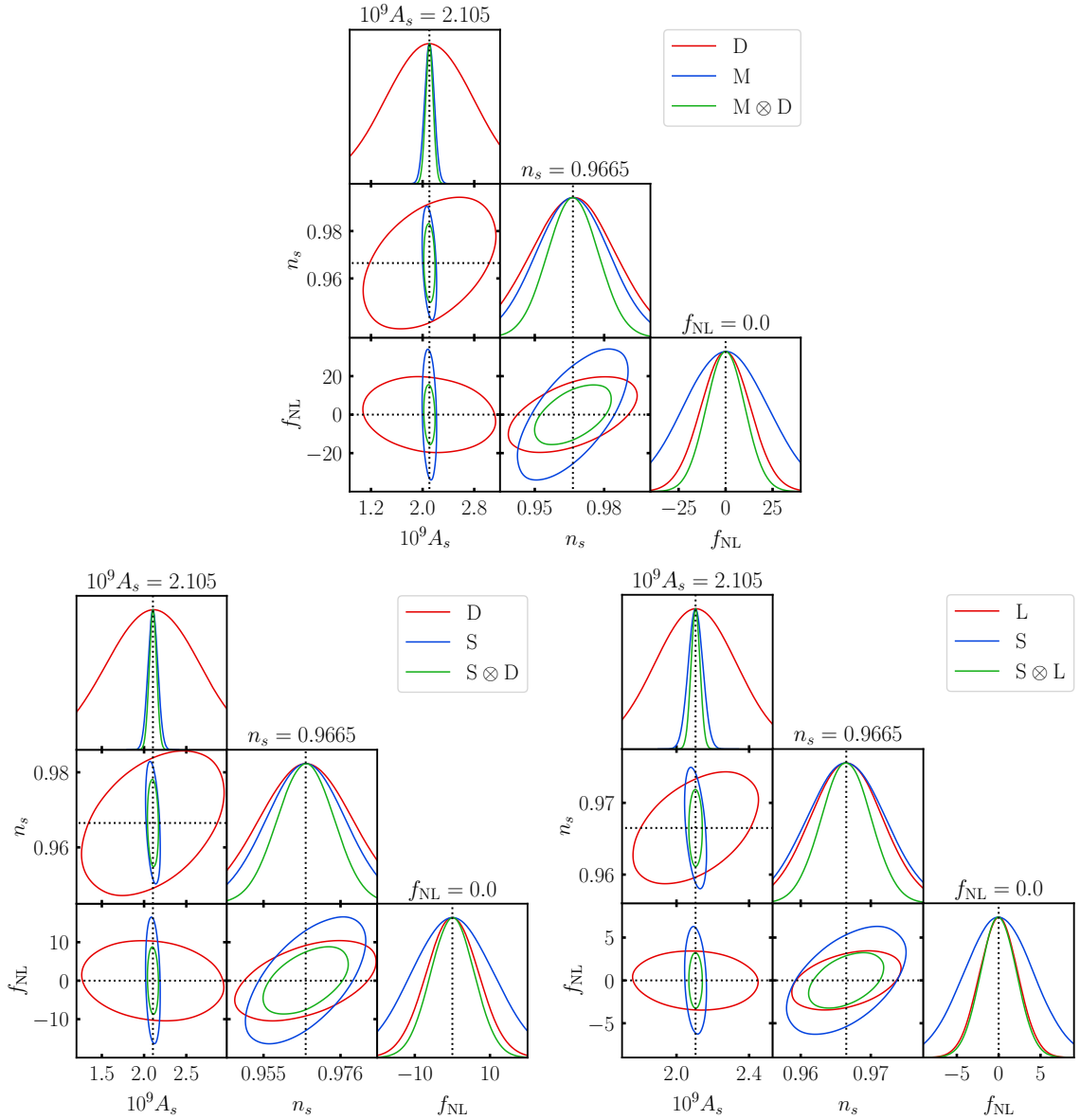


**Figure 7.**  $1\sigma$  (68%CL) contours for the cosmological parameters, marginalised over the nuisance parameters, in the case of HI intensity mapping in single-dish mode combined with photometric redshift surveys, and with  $k_{\text{FG}} = 0.005; h; \text{Mpc}^{-1}$ .

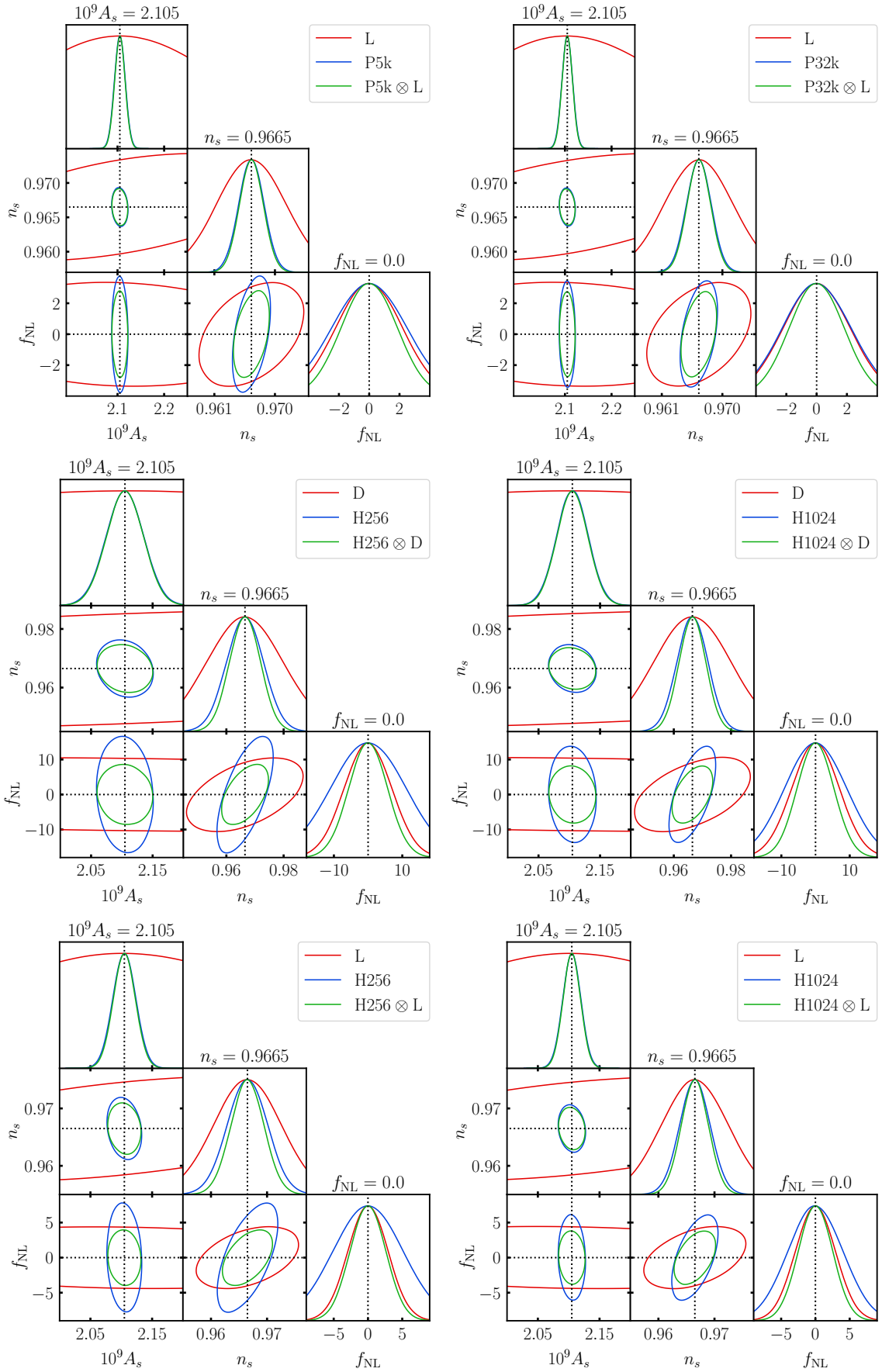


**Figure 8.** As in Figure 7 for the case of  $\mathbb{H}_3$  intensity maps in interferometer mode.

## 7 Conclusions

Our analysis shows that combining HI intensity maps and photometric samples allows us to leverage the strengths of both, suppressing the cosmic variance on very large scales, which is an obstacle to precision constraints on local PNG. We emphasise that our goal was not to produce realistic forecasts and develop methods for optimising future measurements. In particular, we were not aiming to find a multi-tracer combination that could achieve  $\sigma(f_{\text{NL}}) < 1$ .

Instead, we aimed to show the qualitative level of improvement in constraints that could be expected from multi-tracing upcoming surveys that combine surveys with high densities – photometric and HI intensity mapping surveys. With the exception of the MeerKAT-DES combination [25] and the SKA-LSST combination [23] (which are consistent with our results), these multi-tracer combinations have not been previously considered, as far as we are aware.

We find that the relative improvement over the best single-tracer constraints (photometric surveys), are as follows.

- DES-like or LSST-like  $\otimes$  SKA-like versus DES-like or LSST-like alone: 16% and 6%, respectively.
- DES-like or LSST-like  $\otimes$  HIRAX-like versus DES-like or LSST-like alone: 18% [H256], 23% [H1024] and 11% [H256], 14% [H1024], respectively.
- LSST-like  $\otimes$  PUMA-like versus LSST-like alone: 17% [P5k], 18% [P32k].

The single-tracer errors in our findings are generally consistent with earlier results, such as those from [38] for HIRAX-like and PUMA-like surveys, and [34, 59, 61] for SKA Band 1, or [59, 75] for SKA Band 1 and the UHF Band of MeerKAT.

We used a simple Fisher forecast, which produces over-optimistic precision. On the other hand, we discarded the non-overlap information from the multi-tracer pairs, which leads to an under-estimate of precision.

We also investigated the significance of the foreground filtering scale in the multi-tracer analysis. We find that the stronger loss of radial modes in HI intensity maps (e.g., at  $k_{\text{fg}} = 0.01 h/\text{Mpc}$ ) has less impact in the multi-tracer case. For instance, when combining LSST-like and HIRAX-like surveys (red and blue solid lines in Figure 6), there is little difference between  $k_{\text{fg}} = 0.01 h/\text{Mpc}$  and  $k_{\text{fg}} = 0.005 h/\text{Mpc}$ , because the overlapping sky area and redshift range provide many of the ultra-large scales where the  $f_{\text{NL}}$  signal is strongest. By contrast, the MeerKAT-like combination with DES-like (Figure 5) is significantly affected by the loss of long modes, due to the smaller overlap in sky area.

For future work, we plan to improve theoretical accuracy by including wide-angle effects (see e.g. [76–78]).

## Acknowledgments

MK and RM are supported by the South African Radio Astronomy Observatory and the National Research Foundation (grant no. 75415). SJ is supported by the Stellenbosch University Astrophysics Research Group fund.

## References

- [1] J. M. Maldacena, *Non-Gaussian features of primordial fluctuations in single field inflationary models*, *JHEP* **05** (2003) 013, [[astro-ph/0210603](#)].
- [2] C. T. Byrnes and K.-Y. Choi, *Review of local non-Gaussianity from multi-field inflation*, *Adv. Astron.* **2010** (2010) 724525, [[arXiv:1002.3110](#)].
- [3] M. Celoria and S. Matarrese, *Primordial Non-Gaussianity*, *Proc. Int. Sch. Phys. Fermi* **200** (2020) 179–215, [[arXiv:1812.08197](#)].
- [4] P. D. Meerburg et al., *Primordial Non-Gaussianity*, [[arXiv:1903.04409](#)].
- [5] N. Dalal, O. Dore, D. Huterer, and A. Shirokov, *The imprints of primordial non-gaussianities on large-scale structure: scale dependent bias and abundance of virialized objects*, *Phys. Rev. D* **77** (2008) 123514, [[arXiv:0710.4560](#)].
- [6] S. Matarrese and L. Verde, *The effect of primordial non-Gaussianity on halo bias*, *Astrophys. J. Lett.* **677** (2008) L77–L80, [[arXiv:0801.4826](#)].
- [7] **Planck** Collaboration, Y. Akrami et al., *Planck 2018 results. IX. Constraints on primordial non-Gaussianity*, *Astron. Astrophys.* **641** (2020) A9, [[arXiv:1905.05697](#)].
- [8] M. Rezaie et al., *Local primordial non-Gaussianity from the large-scale clustering of photometric DESI luminous red galaxies*, *Mon. Not. Roy. Astron. Soc.* **532** (2024), no. 2 1902–1928, [[arXiv:2307.01753](#)].
- [9] **Simons Observatory** Collaboration, P. Ade et al., *The Simons Observatory: Science goals and forecasts*, *JCAP* **02** (2019) 056, [[arXiv:1808.07445](#)].
- [10] **CMB-S4** Collaboration, K. N. Abazajian et al., *CMB-S4 Science Book, First Edition*, [[arXiv:1610.02743](#)].
- [11] R. de Putter, J. Gleyzes, and O. Doré, *Next non-Gaussianity frontier: What can a measurement with  $\sigma(fNL) \lesssim 1$  tell us about multifield inflation?*, *Phys. Rev. D* **95** (2017), no. 12 123507, [[arXiv:1612.05248](#)].
- [12] **DESI** Collaboration, D. J. Schlegel et al., *A Spectroscopic Road Map for Cosmic Frontier: DESI, DESI-II, Stage-5*, [[arXiv:2209.03585](#)].
- [13] **Euclid** Collaboration, Y. Mellier et al., *Euclid. I. Overview of the Euclid mission*, [[arXiv:2405.13491](#)].
- [14] **SKA** Collaboration, D. J. Bacon et al., *Cosmology with Phase 1 of the Square Kilometre Array: Red Book 2018: Technical specifications and performance forecasts*, *Publ. Astron. Soc. Austral.* **37** (2020) e007, [[arXiv:1811.02743](#)].
- [15] D. Crichton et al., *Hydrogen Intensity and Real-Time Analysis Experiment: 256-element array status and overview*, *J. Astron. Telesc. Instrum. Syst.* **8** (2022) 011019, [[arXiv:2109.13755](#)].
- [16] **PUMA** Collaboration, A. Slosar et al., *Packed Ultra-wideband Mapping Array (PUMA): A Radio Telescope for Cosmology and Transients*, *Bull. Am. Astron. Soc.* **51** (2019) 53, [[arXiv:1907.12559](#)].
- [17] D. Alonso, P. Bull, P. G. Ferreira, R. Maartens, and M. Santos, *Ultra large-scale cosmology in next-generation experiments with single tracers*, *Astrophys. J.* **814** (2015) 145, [[arXiv:1505.07596](#)].
- [18] A. Raccanelli, F. Montanari, D. Bertacca, O. Doré, and R. Durrer, *Cosmological Measurements with General Relativistic Galaxy Correlations*, *JCAP* **05** (2016) 009, [[arXiv:1505.06179](#)].
- [19] U. Seljak, *Extracting primordial non-gaussianity without cosmic variance*, *Phys. Rev. Lett.* **102** (2009) 021302, [[arXiv:0807.1770](#)].



- [20] P. McDonald and U. Seljak, *How to measure redshift-space distortions without sample variance*, *JCAP* **10** (2009) 007, [[arXiv:0810.0323](#)].
- [21] L. D. Ferramacho, M. G. Santos, M. J. Jarvis, and S. Camera, *Radio galaxy populations and the multitracers technique: pushing the limits on primordial non-Gaussianity*, *Mon. Not. Roy. Astron. Soc.* **442** (2014), no. 3 2511–2518, [[arXiv:1402.2290](#)].
- [22] D. Yamauchi, K. Takahashi, and M. Oguri, *Constraining primordial non-Gaussianity via a multitracers technique with surveys by Euclid and the Square Kilometre Array*, *Phys. Rev. D* **90** (2014), no. 8 083520, [[arXiv:1407.5453](#)].
- [23] D. Alonso and P. G. Ferreira, *Constraining ultralarge-scale cosmology with multiple tracers in optical and radio surveys*, *Phys. Rev. D* **92** (2015), no. 6 063525, [[arXiv:1507.03550](#)].
- [24] J. Fonseca, S. Camera, M. Santos, and R. Maartens, *Hunting down horizon-scale effects with multi-wavelength surveys*, *Astrophys. J.* **812** (2015), no. 2 L22, [[arXiv:1507.04605](#)].
- [25] J. Fonseca, R. Maartens, and M. G. Santos, *Probing the primordial Universe with MeerKAT and DES*, *Mon. Not. Roy. Astron. Soc.* **466** (2017), no. 3 2780–2786, [[arXiv:1611.01322](#)].
- [26] J. Fonseca, R. Maartens, and M. G. Santos, *Synergies between intensity maps of hydrogen lines*, *Mon. Not. Roy. Astron. Soc.* **479** (2018), no. 3 3490–3497, [[arXiv:1803.07077](#)].
- [27] A. Witzemann, D. Alonso, J. Fonseca, and M. G. Santos, *Simulated multitracers analyses with  $H\text{ I}$  intensity mapping*, *Mon. Not. Roy. Astron. Soc.* **485** (2019), no. 4 5519–5531, [[arXiv:1808.03093](#)].
- [28] M. Ballardini, W. L. Matthews, and R. Maartens, *Constraining primordial non-Gaussianity using two galaxy surveys and CMB lensing*, *Mon. Not. Roy. Astron. Soc.* **489** (2019), no. 2 1950–1956, [[arXiv:1906.04730](#)].
- [29] D. Ginzburg and V. Desjacques, *Shot noise in multitracers constraints on  $f_{\text{NL}}$  and relativistic projections: Power spectrum*, *Mon. Not. Roy. Astron. Soc.* **495** (2020), no. 1 932–942, [[arXiv:1911.11701](#)].
- [30] Z. Gomes, S. Camera, M. J. Jarvis, C. Hale, and J. Fonseca, *Non-Gaussianity constraints using future radio continuum surveys and the multitracers technique*, *Mon. Not. Roy. Astron. Soc.* **492** (2020) 1513, [[arXiv:1912.08362](#)].
- [31] J.-A. Viljoen, J. Fonseca, and R. Maartens, *Multi-wavelength spectroscopic probes: prospects for primordial non-Gaussianity and relativistic effects*, *JCAP* **11** (2021) 010, [[arXiv:2107.14057](#)].
- [32] J.-A. Viljoen, J. Fonseca, and R. Maartens, *Multi-wavelength spectroscopic probes: biases from neglecting light-cone effects*, *JCAP* **12** (2021), no. 12 004, [[arXiv:2108.05746](#)].
- [33] S. Casas, I. P. Carucci, V. Pettorino, S. Camera, and M. Martinelli, *Constraining gravity with synergies between radio and optical cosmological surveys*, *Phys. Dark Univ.* **39** (2023) 101151, [[arXiv:2210.05705](#)].
- [34] S. Jolicoeur, R. Maartens, and S. Dlamini, *Constraining primordial non-Gaussianity by combining next-generation galaxy and 21 cm intensity mapping surveys*, *Eur. Phys. J. C* **83** (2023), no. 4 320, [[arXiv:2301.02406](#)].
- [35] A. Barreira and E. Krause, *Towards optimal and robust  $f_{\text{NL}}$  constraints with multi-tracer analyses*, *JCAP* **10** (2023) 044, [[arXiv:2302.09066](#)].
- [36] J. M. Sullivan, T. Prijon, and U. Seljak, *Learning to concentrate: multi-tracer forecasts on local primordial non-Gaussianity with machine-learned bias*, *JCAP* **08** (2023) 004, [[arXiv:2303.08901](#)].
- [37] M. B. Squarotti, S. Camera, and R. Maartens, *Radio-optical synergies at high redshift to constrain primordial non-Gaussianity*, *JCAP* **02** (2024) 043, [[arXiv:2307.00058](#)].

- [38] M. Kopana, S. Jolicoeur, and R. Maartens, *Multi-tracing the primordial Universe with future surveys*, *Eur. Phys. J. C* **84** (2024), no. 5 491, [[arXiv:2312.12994](#)].
- [39] D. J. Schlegel et al., *The MegaMapper: A Stage-5 Spectroscopic Instrument Concept for the Study of Inflation and Dark Energy*, [arXiv:2209.04322](#).
- [40] **MeerKLASS** Collaboration, M. G. Santos et al., *MeerKLASS: MeerKAT Large Area Synoptic Survey*, in *MeerKAT Science: On the Pathway to the SKA*, 9, 2017. [arXiv:1709.06099](#).
- [41] **DES** Collaboration, T. M. C. Abbott et al., *Dark Energy Survey Year 3 results: Cosmological constraints from galaxy clustering and weak lensing*, *Phys. Rev. D* **105** (2022), no. 2 023520, [[arXiv:2105.13549](#)].
- [42] **LSST** Collaboration, v. Ivezić et al., *LSST: from Science Drivers to Reference Design and Anticipated Data Products*, *Astrophys. J.* **873** (2019), no. 2 111, [[arXiv:0805.2366](#)].
- [43] A. G. Adame, S. Avila, V. Gonzalez-Perez, G. Yepes, M. Pellejero, M. S. Wang, C.-H. Chuang, Y. Feng, J. Garcia-Bellido, and A. Knebe, *PNG-UNITsims: Halo clustering response to primordial non-Gaussianities as a function of mass*, *Astron. Astrophys.* **689** (2024) A69, [[arXiv:2312.12405](#)].
- [44] A. Barreira, G. Cabass, F. Schmidt, A. Pillepich, and D. Nelson, *Galaxy bias and primordial non-Gaussianity: insights from galaxy formation simulations with IllustrisTNG*, *JCAP* **12** (2020) 013, [[arXiv:2006.09368](#)].
- [45] A. Barreira, *The local PNG bias of neutral Hydrogen, HI*, *JCAP* **04** (2022), no. 04 057, [[arXiv:2112.03253](#)].
- [46] A. Barreira, *Can we actually constrain  $f_{NL}$  using the scale-dependent bias effect? An illustration of the impact of galaxy bias uncertainties using the BOSS DR12 galaxy power spectrum*, *JCAP* **11** (2022) 013, [[arXiv:2205.05673](#)].
- [47] E. Fondi, L. Verde, F. Villaescusa-Navarro, M. Baldi, W. R. Coulton, G. Jung, D. Karagiannis, M. Liguori, A. Ravenni, and B. D. Wandelt, *Taming assembly bias for primordial non-Gaussianity*, *JCAP* **02** (2024) 048, [[arXiv:2311.10088](#)].
- [48] **Planck** Collaboration, N. Aghanim et al., *Planck 2018 results. VI. Cosmological parameters*, *Astron. Astrophys.* **641** (2020) A6, [[arXiv:1807.06209](#)]. [Erratum: *Astron. Astrophys.* 652, C4 (2021)].
- [49] H.-J. Seo and D. J. Eisenstein, *Probing dark energy with baryonic acoustic oscillations from future large galaxy redshift surveys*, *Astrophys. J.* **598** (2003) 720–740, [[astro-ph/0307460](#)].
- [50] H. Zhan and L. Knox, *Baryon oscillations and consistency tests for photometrically-determined redshifts of very faint galaxies*, *Astrophys. J.* **644** (2006) 663–670, [[astro-ph/0509260](#)].
- [51] D. Green, Y. Guo, J. Han, and B. Wallisch, *Light fields during inflation from BOSS and future galaxy surveys*, *JCAP* **05** (2024) 090, [[arXiv:2311.04882](#)].
- [52] S. Cunnington, S. Camera, and A. Pourtsidou, *The degeneracy between primordial non-Gaussianity and foregrounds in 21 cm intensity mapping experiments*, *Mon. Not. Roy. Astron. Soc.* **499** (2020), no. 3 4054–4067, [[arXiv:2007.12126](#)].
- [53] S. Cunnington, C. Watkinson, and A. Pourtsidou, *The  $H\text{i}$  intensity mapping bispectrum including observational effects*, *Mon. Not. Roy. Astron. Soc.* **507** (2021), no. 2 1623–1639, [[arXiv:2102.11153](#)].
- [54] M. Spinelli, I. P. Carucci, S. Cunnington, S. E. Harper, M. O. Irfan, J. Fonseca, A. Pourtsidou, and L. Wolz, *SKAO  $H\text{i}$  intensity mapping: blind foreground subtraction challenge*, *Mon. Not. Roy. Astron. Soc.* **509** (2021), no. 2 2048–2074, [[arXiv:2107.10814](#)].
- [55] S. Cunnington et al., *The foreground transfer function for  $H\text{i}$  intensity mapping signal*

reconstruction: MeerKLASS and precision cosmology applications, *Mon. Not. Roy. Astron. Soc.* **523** (2023), no. 2 2453–2477, [[arXiv:2302.07034](#)].

- [56] J. C. Pober et al., *What Next-Generation 21 cm Power Spectrum Measurements Can Teach Us About the Epoch of Reionization*, *Astrophys. J.* **782** (2014) 66, [[arXiv:1310.7031](#)].
- [57] J. C. Pober, *The Impact of Foregrounds on Redshift Space Distortion Measurements With the Highly-Redshifted 21 cm Line*, *Mon. Not. Roy. Astron. Soc.* **447** (2015), no. 2 1705–1712, [[arXiv:1411.2050](#)].
- [58] A. Obuljen, E. Castorina, F. Villaescusa-Navarro, and M. Viel, *High-redshift post-reionization cosmology with 21cm intensity mapping*, *JCAP* **05** (2018) 004, [[arXiv:1709.07893](#)].
- [59] D. Alonso, P. G. Ferreira, M. J. Jarvis, and K. Moodley, *Calibrating photometric redshifts with intensity mapping observations*, *Phys. Rev. D* **96** (2017), no. 4 043515, [[arXiv:1704.01941](#)].
- [60] A. Ghosh, F. Mertens, and L. V. E. Koopmans, *Deconvolving the wedge: maximum-likelihood power spectra via spherical-wave visibility modelling*, *Mon. Not. Roy. Astron. Soc.* **474** (2018), no. 4 4552–4563, [[arXiv:1709.06752](#)].
- [61] D. Karagiannis, A. Slosar, and M. Liguori, *Forecasts on Primordial non-Gaussianity from 21 cm Intensity Mapping experiments*, *JCAP* **11** (2020) 052, [[arXiv:1911.03964](#)].
- [62] D. Blas, J. Lesgourgues, and T. Tram, *The Cosmic Linear Anisotropy Solving System (CLASS) II: Approximation schemes*, *JCAP* **1107** (2011) 034, [[arXiv:1104.2933](#)].
- [63] N. Agarwal, V. Desjacques, D. Jeong, and F. Schmidt, *Information content in the redshift-space galaxy power spectrum and bispectrum*, *JCAP* **03** (2021) 021, [[arXiv:2007.04340](#)].
- [64] F. Villaescusa-Navarro et al., *Ingredients for 21 cm Intensity Mapping*, *Astrophys. J.* **866** (2018), no. 2 135, [[arXiv:1804.09180](#)].
- [65] **DES** Collaboration, C. Bonnett et al., *Redshift distributions of galaxies in the Dark Energy Survey Science Verification shear catalogue and implications for weak lensing*, *Phys. Rev. D* **94** (2016), no. 4 042005, [[arXiv:1507.05909](#)].
- [66] E. Castorina and F. Villaescusa-Navarro, *On the spatial distribution of neutral hydrogen in the Universe: bias and shot-noise of the HI power spectrum*, *Mon. Not. Roy. Astron. Soc.* **471** (2017), no. 2 1788–1796, [[arXiv:1609.05157](#)].
- [67] J.-A. Viljoen, J. Fonseca, and R. Maartens, *Constraining the growth rate by combining multiple future surveys*, *JCAP* **09** (2020) 054, [[arXiv:2007.04656](#)].
- [68] P. Bull, P. G. Ferreira, P. Patel, and M. G. Santos, *Late-time cosmology with 21cm intensity mapping experiments*, *Astrophys. J.* **803** (2015), no. 1 21, [[arXiv:1405.1452](#)].
- [69] S. Jolicoeur, R. Maartens, E. M. De Weerd, O. Umeh, C. Clarkson, and S. Camera, *Detecting the relativistic bispectrum in 21cm intensity maps*, *JCAP* **06** (2021) 039, [[arXiv:2009.06197](#)].
- [70] E. Castorina et al., *Packed Ultra-wideband Mapping Array (PUMA): Astro2020 RFI Response*, [[arXiv:2002.05072](#)].
- [71] M. White, Y.-S. Song, and W. J. Percival, *Forecasting Cosmological Constraints from Redshift Surveys*, *Mon. Not. Roy. Astron. Soc.* **397** (2008) 1348–1354, [[arXiv:0810.1518](#)].
- [72] G.-B. Zhao et al., *The completed SDSS-IV extended Baryon Oscillation Spectroscopic Survey: a multitracers analysis in Fourier space for measuring the cosmic structure growth and expansion rate*, *Mon. Not. Roy. Astron. Soc.* **504** (2021), no. 1 33–52, [[arXiv:2007.09011](#)].
- [73] A. Barreira, *On the impact of galaxy bias uncertainties on primordial non-Gaussianity constraints*, *JCAP* **12** (2020) 031, [[arXiv:2009.06622](#)].
- [74] D. Karagiannis, R. Maartens, J. Fonseca, S. Camera, and C. Clarkson, *Multi-tracer power spectra and bispectra: formalism*, *JCAP* **03** (2024) 034, [[arXiv:2305.04028](#)].

- [75] D. Karagiannis, J. Fonseca, R. Maartens, and S. Camera, *Probing primordial non-Gaussianity with the power spectrum and bispectrum of future 21 cm intensity maps*, *Phys. Dark Univ.* **32** (2021) 100821, [[arXiv:2010.07034](#)].
- [76] M. Noorikuhani and R. Scoccimarro, *Wide-angle and relativistic effects in Fourier-space clustering statistics*, *Phys. Rev. D* **107** (2023), no. 8 083528, [[arXiv:2207.12383](#)].
- [77] P. Paul, C. Clarkson, and R. Maartens, *Wide-angle effects in multi-tracer power spectra with Doppler corrections*, *JCAP* **04** (2023) 067, [[arXiv:2208.04819](#)].
- [78] S. Jolicoeur, S. L. Guedezounme, R. Maartens, P. Paul, C. Clarkson, and S. Camera, *Relativistic and wide-angle corrections to galaxy power spectra*, *JCAP* **08** (2024) 027, [[arXiv:2406.06274](#)].